Editors' Suggestion

Diamond-based magnetometer aboard the International Space Station

Yarne Beerden,[1,2] Boo Carmans,[1,2] Remy Vandebosch,[1,2] Dries Hendrikx,[1] Sam Bammens,[1] Musa Aydogan,[1] Siemen Achten,[1] Jeffrey Gorissen,[1] Sebastiaan Vanspauwen,[1] Siemen Vandervoort,[1] Teoman Köseoglu,[1] Jens Mannaerts,[1] Stijn Jacobs,[1] Daphne Box,[1] Milos Nesladek,[1,2] and Jaroslav Hruby[1,2,*]

[1] *Hasselt University, Institute for Materials Research (IUMAT), Martelarenlaan 42, B-3500 Hasselt, Belgium*
[2] *imec, IUMAT, Wetenschapspark 1, B-3590 Diepenbeek, Belgium*

(Received 10 September 2025; revised 20 January 2026; accepted 3 March 2026; published 7 May 2026)

Precise mapping of the geomagnetic field is essential for understanding Earth's geodynamics, space weather interactions, and navigation applications. Traditional magnetometers face limitations in sensitivity for a wide dynamic range, and compactness. To address these challenges, the OSCAR-QUBE quantum magnetometer based on nitrogen-vacancy centers in diamond was developed, providing a sensitive and compact solution for space-based magnetic-field measurements. Our system employs optically detected magnetic resonance to measure magnetic fields utilizing the quantum properties of nitrogen-vacancy centers in a miniaturized design. The form factor of the final device was 1U ($10 \times 10 \times 10\,\mathrm{cm}^3$), weighing 420 g, and had a power consumption of 5 W. Deployed aboard the International Space Station, our magnetometer measured high-resolution magnetic-field maps, achieving a sensitivity of $<300\,\mathrm{nT}/\sqrt{\mathrm{Hz}}$ and successfully demonstrating *in situ* vector magnetic-field mapping under low-Earth-orbit conditions. These results validate the flight-proven application of diamond quantum sensing in space, demonstrating the feasibility of solid-state quantum magnetometry for next-generation remote sensing and Earth observation missions. This work lays the foundation for future compact, multisensor quantum payloads for both scientific and commercial space applications.

DOI: 10.1103/483m-8hfc

I. INTRODUCTION

Magnetic-field measurements in space provide insight into geomagnetic dynamics, planetary formation, and various geological processes [1]. Earth's magnetic field plays a crucial role, acting as a protective shield against solar radiation. High-precision magnetometry offers a deeper understanding of the dynamic behavior of the magnetic field and its interaction with space weather phenomena [2]. Furthermore, geomagnetic data collected from space supports technological advancements in satellite navigation and enhances the reliability of satellite systems by monitoring environmental conditions that affect onboard sensors [3,4].

As such, space magnetometry has received significant global attention due to its role in advancing our understanding of Earth's magnetic environment and supporting the operational demands of modern space missions. Currently the primary mission measuring the magnetic field of Earth from space is ESA Swarm [5]. This constellation consists of three identical satellites equipped with a high-precision vector-field magnetometer and an absolute scalar magnetometer, enabling measurements of both direction and intensity of the Earth's magnetic field [6,7]. This approach of multiple sensors allows for enhanced accuracy and increased reliability while being able to calibrate the sensors. Other Earth magnetometry missions such as CSES [8] and MSS-1 [9], and upcoming missions NanoMagSat [10,11] and NASA's MagQuest [12] demonstrate the significance of gathering high-precision magnetic-field measurements on miniaturized, CubeSat-sized platforms. These initiatives are targeting large constellations of magnetometers measuring Earth's magnetic field simultaneously while offering higher temporal and spatial resolution of the magnetic-field variations. Data collected by such missions contributes to geomagnetic field models such as CHAOS (CHAMP, Ørsted, and SAC-C model of Earth's magnetic field) [13] and international geomagnetic reference field (IGRF) [14].

There are several challenges involved in measuring magnetic fields in space, primarily due to the harsh

*Contact author: jaroslav.hruby@uhasselt.be

operational environment and constraints imposed by the satellite platform. Spacecraft-generated electromagnetic noise requires the use of a deployable boom or magnetic gradiometry to remove the magnetometer from onboard interference sources and increase measurement accuracy [15,16]. Additionally, sensors must be designed to withstand harsh conditions such as thermal variations and cycling, high-energy ionizing radiation, microgravity, and (micro)vibrations [15,17]. All these factors impact long-term performance of the sensor due to degradation or drift of the calibration [18,19]. Thus, onboard calibration is required for every space mission utilizing a magnetometer payload. While this has been successfully implemented in current fluxgate magnetometers, maintaining calibration accuracy remains a significant challenge limiting overall measurement precision [20,21]. Fluxgate sensors offer strong heritage and sensitivity, but they are susceptible to offset and scale-factor drift with temperature and ageing, and to hysteresis effects, which drive periodic recalibration and careful magnetic cleanliness requirements [15]. In contrast, miniaturized microelectromechanical system (MEMS) magnetometers offer excellent size, weight, and power consumption (SWaP), but exhibit higher noise floors and stronger temperature-dependent offset and scale-factor drifts. This can limit absolute accuracy in precision applications without frequent calibration and compensation [15]. As such there is an increased demand for magnetometers with reduced SWaP while remaining sensitive and complying to Earth observation (EO) requirements. This is due to an increasing popularity of smaller platforms, particularly CubeSats [15,22]. Classical sensors, however, are approaching their fundamental performance limits in terms of both SWaP and sensitivity to magnetic fields [15]. This calls for innovative sensing solutions and performance optimization approaches to enable miniaturized magnetometers capable of meeting modern space-mission requirements.

A promising emerging technology for space magnetometry is based on nitrogen-vacancy (NV) centers in diamond. These sensors address key limitations of existing platforms by combining high sensitivity [23] with robustness to the environment. Diamonds' inherent radiation hardness, thermal stability, and mechanical robustness make it well suited for harsh space environment operation [24]. NV-based magnetometers offer a wide dynamic range (linear up to 0.1 T) [25,26], broad bandwidth (dc–MHz) [25,26], and vector-field-sensing capabilities [27], while also enabling simultaneous temperature measurements [28]. Recent advancements have demonstrated subnanotesla sensitivities using compact implementations, approaches include fiber-based readout, LED excitation, and CMOS integration [29–34]. However, most of these efforts remain at the sensor-head level, lacking full system integration. This presents a challenge for space applications, which require compact, low SWaP, and fully integrated devices capable of long-term autonomous operation.

In this work we present miniaturization efforts leading to the development of a fully integrated NV-based magnetometer prototype, as part of the Optical Sensors based on CARbon materials: QUantum BElgium (OSCAR-QUBE) mission. OSCAR is an interdisciplinary student team developing miniaturized quantum sensors based on diamond. The main goal is to miniaturize and further integrate this technology to prepare it for space applications, while allowing students to step into the fields of quantum and space research. The OSCAR-QUBE device is a 1U NV magnetometer achieving measured sensitivity of $<300\,\mathrm{nT}/\sqrt{\mathrm{Hz}}$ using continuous-wave optically detected magnetic resonance (cw ODMR). The sensor was deployed aboard the International Space Station (ISS), operating in low-Earth-orbit conditions. This marks the first demonstration of a fully integrated portable NV diamond-based magnetometer successfully tested in space, where it measured and mapped Earth's magnetic field from aboard the ISS [35,36]. Although the device's sensitivity was lower than that of state-of-the-art benchtop systems at the time, it was still able to measure the magnetic field with high precision and verify its readings against geomagnetic models. Based on the data acquired during its 10 months' operation the stability and sensitivity of the sensor are evaluated. This work demonstrates the successful operation of a diamond-based sensor for 10 months in a space environment. The in-orbit performance and future improvement strategies are discussed and outlined.

II. MATERIALS AND METHODS

A. NV-based magnetometry

The operational principle of the NV-based magnetometer relies on optomagnetically active defects in the diamond crystal lattice called nitrogen-vacancy centers. These defects consist of a substitutional nitrogen atom (N) adjacent to a lattice vacancy (V) [37]. NV centers possess a negatively charged state that exhibits spin-dependent photoluminescence (PL), enabling ODMR to be used for magnetic-field sensing [38]. Upon excitation with green laser light (typically 532 nm), the NV^- centers emit red photoluminescence (>637 nm). The application of microwaves (MWs), via an antenna near the diamond surface, at a frequency resonant with the NV spin transitions allows for controlled spin-state manipulation. In the NV ground state, the spin sublevels $m_S = 0$ (bright state) and $m_S = \pm 1$ (dark state) have distinct fluorescence properties due to the presence of a nonradiative metastable state involved in the relaxation process. The external magnetic field can be measured via the Zeeman effect, where the $m_S = \pm 1$ states split symmetrically, shifting the resonant microwave frequencies proportionally to the field

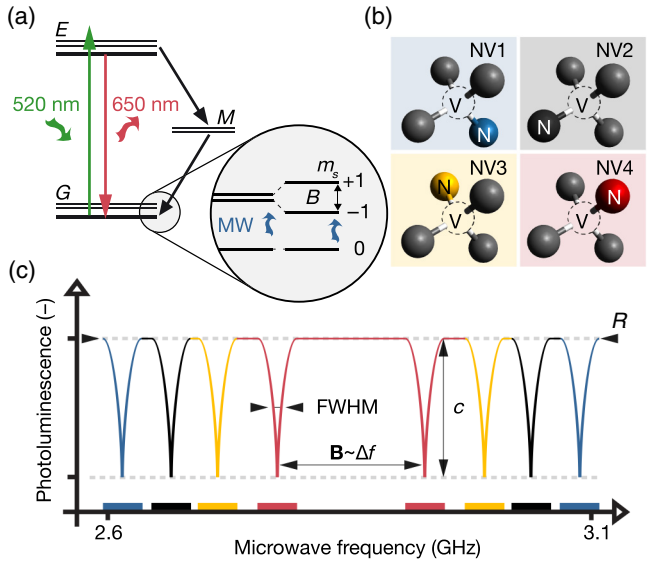

FIG. 1. (a) Energy-level diagram of the negatively charged NV center, showing the spin sublevels m_S within the ground state (G), excited state (E), and metastable state (M). (b) Illustration of the four possible NV-center orientations (NV1, NV2, NV3, NV4) within the tetrahedral crystal lattice of diamond, which are essential for vector magnetometry. (c) Example ODMR spectrum showing four pairs of peaks corresponding to the four NV-center orientations. Key parameters that affect sensitivity are highlighted: the FWHM, contrast c, and photon count rate R. The positions of the ODMR resonances are influenced by both intrinsic crystal properties and external conditions, such as magnetic field and temperature.

strength (Fig. 1). NV centers are oriented along one of the four tetrahedral axes in the diamond lattice, allowing for three-dimensional (3D) vector magnetometry. In this work, cw ODMR [25] is used to perform magnetic-field measurements. However, more advanced measurements can be achieved by pulsed mode operation (modulating the laser and microwave in a defined sequence) to directly manipulate the spin states of the NV centers [39]. ODMR can be used to measure both magnetic field and temperature: the Zeeman splitting (difference of the ± transitions) gives the magnetic field, while the common shift of both resonances (ZFS) reflects temperature. A complementary technique to ODMR, that can serve as a possible further improvement, is called photocurrent detected magnetic resonance (PDMR) [40–43]. While the final device was PDMR capable, it was not utilized during the mission due to final diamond sample selection.

NV-based magnetic-field sensors demonstrated detecting magnetic fields down to the pT range [44,45], by leveraging the spin-dependent PL properties of NV centers. The sensitivity is theoretically constrained by spin coherence times T_2^*, photon shot noise, and ODMR contrast. The theoretical cw sensitivity for the system is determined by Ref. [25]:

$$\eta_{\mathrm{cw}} = \frac{4}{3\sqrt{3}} \times \frac{h}{g\mu_B} \times \frac{\Delta\nu}{C\sqrt{R}}, \tag{1}$$

where C is ODMR contrast, R the rate of detected photons, $\Delta\nu$ the spin resonance linewidth, h Planck's constant, g the g factor of NV electron spin, and μ_B is Bohr's magneton. By tuning these parameters, the sensitivity can be optimized. The laser power influences the spin-state initialization and readout, affecting R. Microwave power influences the resonance linewidth and contrast. The detection efficiency (e.g., photodiode, optics) affects the signal-to-noise ratio (SNR). The sensitivity is further influenced by the homogeneity of the applied microwave field, and the spot size and stability of the green laser. A high-density NV-center ensemble was selected for this mission to maximize PL signal, increasing the SNR and sensitivity. Besides this, sensitivity can be increased by shielding, data processing, and further optimization of the hardware systems. The diamond sample used was a CVD, electron irradiated sample with average nitrogen concentration of 14 ppm, NV concentration of 2 ppm, FWHM of 100 kHz, and lattice-plane orientation of 100 provided by Element Six.

B. Sensor configuration

The overall sensor layout is shown in Fig. 2. It consists of four printed circuit boards (PCBs) layered on top of each other separated by aluminium spacers. The bottommost board contains the control and power subsystem including the field programmable gate array (FPGA). It also contains the reference MEMS magnetic-field sensor (LSM303AGR, STMicroelectronics). The second layer contains the laser subsystem and the laser housing, designed with dual purpose as both laser heatsink and for focusing of the laser beam on the diamond sample. The third layer contains the diamond, microwave electronics and photocurrent readout electronics. An armlike mount with a permanent $5 \times 5 \times 1.2\,\mathrm{mm}^3$ Neodymium (NdFeB) magnet mounted is placed in close proximity to induce Zeeman splitting and minimize magnetic-field perturbations to the surroundings. The mechanical stability of the arm was tested and characterized before the mission. Both the placement, strength, and positional stability of the bias permanent magnet are key to ensure uniform splitting required for vector measurements. The top-most board contains the optical readout system to measure the photoluminescence emitted from the diamond located on the third board. The microwave line antenna was positioned above the diamond surface. The laser was aligned to be as close as possible to the antenna, where the generated microwave field was quasiuniform. The optical path of the system was designed to maximize the collection efficiency for the red PL. The design was chosen for both

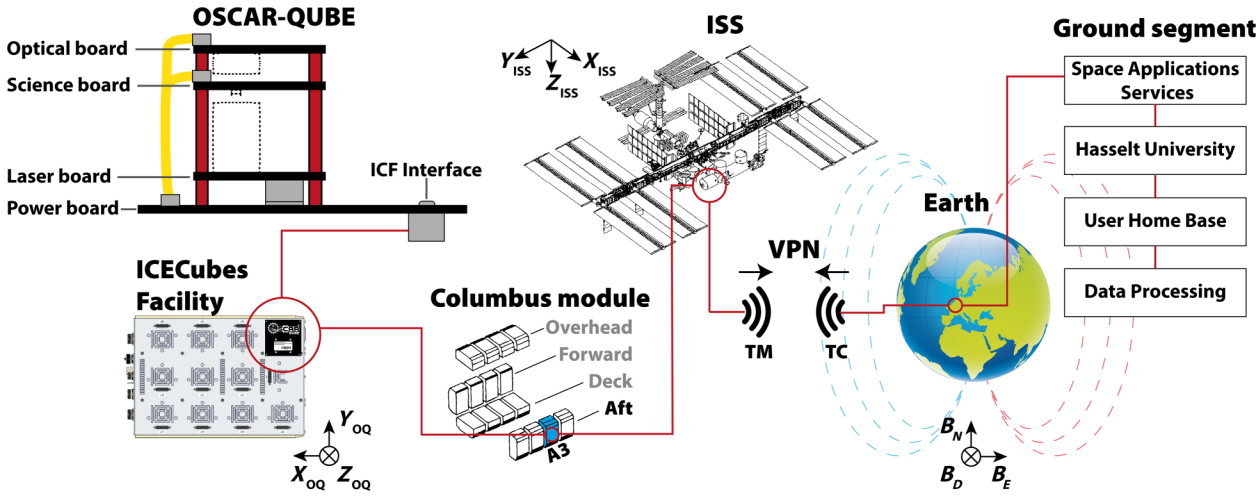

FIG. 2. Ecosystem of the OSCAR-QUBE mission, showing the diamond magnetometer integrated into the ICECubes Facility within the Columbus module aboard the International Space Station. Data is transmitted to Earth through a secure VPN connection to Space Application Services, stored and processed by the User Home Base part of the ground segment at Hasselt University. Magnetic-field measurements are transformed into Earth-fixed coordinates for scientific analysis.

compactness, further miniaturization, and with modularity in mind. The mechanical alignment of the full optical path is fixed by the housing and was verified to be stable before and after vibration and thermal-vacuum testing, with no measurable change in the calibration. The specific layout was also influenced by the SWaP constraints imposed by its deployment aboard the ISS (see below). The system layout was specifically designed to minimize the electromagnetic interference between subsystems and the diamond or other components. Based on approximations, the impact of these subsystems in the worst-case scenario was below the sensitivity limit of the sensor. Furthermore, key aspects to consider during the design phase were both thermal and mechanical stability. Thermal management was focused on the mitigation of noise in the data caused by thermal effects and heating variations. The main heat sources, such as laser and microwave components, were modeled to better understand and analyze the thermal behavior and optimize their placement. The laser housing itself acts as a heatsink to dissipate excess heat generated by the laser during the experiment. The use of an aluminum shell and aluminum standoffs contributed to improved thermal conduction and structural stability. Rigorous testing was performed preflight to ensure the device remained stable during the mission duration. The final system, as described above, was contained in 1U ($10 \times 10 \times 10\,\mathrm{cm}^3$) and weighed 420 g. In-depth description of the integration and miniaturization can be found in previous works [35,36].

The laser diode's (520 nm) optical power was adjustable up to 53 mW, allowing for adjustments in power to optimize the excitation of NV centers. Microwave power was adjustable from −6 to +26 dBm, with a maximum sweep range from 2600–3200 MHz. After an initial phase of inflight optimization at the start of commissioning, all adjustable parameters were fixed. This process of parameter optimization was repeated several times during the mission duration.

C. Mission ecosystem

The mission was performed within the framework of the ESA Academy Experiments program "Orbit Your Thesis!" (OYT) designed for guiding students through the design, development, testing, and operations of experiments aboard the ISS housed inside the ICECubes Facility (ICF, Space Applications Services). The ICF is housed in the EPM rack inside the European module Columbus. The ecosystem is shown in Fig. 2. While the program enabled access to space, it imposed strict constraints to ensure compliance with the ISS's operational and safety requirements. The payload operated within ICF, defining constraints on SWaP. The form factor was limited to CubeSat standards (e.g., 1U–2U), with power lines (5 and 12 V) and mass budgets. Thermal management was provided by the ICF, which was controlled between 20 and 25 °C. Additional radiation shielding by the ISS reduced the need for radiation-hardened components. Human-rated safety standards imposed further limitations to mitigate failure propagation. No information was provided about the magnetic cleanliness environment aboard the ISS. The payload had a continuous connection to the user home base via a VPN, resulting in around 231 GB of measurement data over the duration of the mission. The sensor was turned off during multiple periods, resulting in gaps in the dataset. The ISS maintains an average orbital altitude of approximately 400–420 km, with an inclination of 51.6°. The average spatial resolution of the sensor was

calculated to be 7.7 km for the downsampled 1 Hz data. The microgravity environment minimized thermal convective effects, potentially influencing sensor performance. The orbital day–night cycle introduces thermal fluctuations in the spacecraft, which can further influence the performance. This cycle also affects the measured magnetic field, as solar radiation drives ionospheric currents that distort the geomagnetic field.

D. Preflight system validation procedures

To verify both the scientific concepts and also the subsystems, a test-bench approach was chosen. This "flat-sat" approach offered a modular system in which the developed subsystems could easily be validated against commercial off-the-shelf (COTS) components. Testing on this test bench during the first phase of the project confirmed the compatibility of the designed subsystem and feasibility for achieving the desired sensitivity for the final sensor. During the testing phase, the device's subsystems were evaluated to ensure adherence to the payload requirements. Final integration was focused on system calibration, stability, and readiness for operation. To ensure that the device would survive the launch to the ISS, extensive qualification tests were performed. These environmental tests included vibration, thermal, and electromagnetic interference testing. Simultaneously, a functionally identical sensor (besides the diamond sample) was developed for on-ground testing and long-term performance evaluation.

E. Data-processing workflow

After the onboard acquisition, the data was formatted into packets and transferred to the User Home Base on ground. The packet contained all the ODMR sweeps, reference magnetometry data, and housekeeping data. The data were then processed following the scheme shown in Fig. 3 to produce magnetic-field maps. ODMR measurements yield resonance frequencies for all four NV orientations, with the peak splittings proportional to the magnetic-field projection along each of the four calibrated NV axes. The splittings are extracted from the ODMR spectra using a peak-detection algorithm, from which the magnetic-field components along the four NV axes are determined. These projections are then combined via a least-squares inversion to reconstruct the 3D magnetic-field vector in the sensor frame. This process is described in detail in Ref. [27].

As seen in Fig. 2, there are multiple reference frames relevant to data interpretation in which the sensor operated. Locally, the magnetic-field data was measured in the sensor's intrinsic reference frame determined by the orientation of the diamond. This reference frame was determined by NV-axes calibration on-ground preflight and remained fixed. As previously stated, the sensor is mounted inside the ICF with a certain reference frame. The ICF is inside the ISS with a reference frame defined by the station's

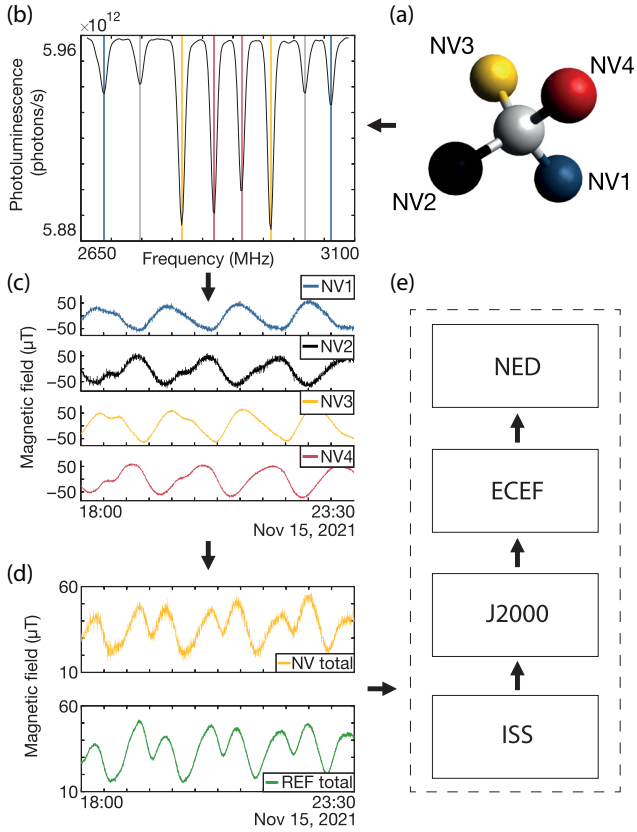

FIG. 3. Data-processing workflow. (a) Schematic simplified representation of NV-center orientation inside diamond lattice. (b) ODMR spectrum measured aboard the ISS, highlighting resonance frequency pairs corresponding to all four NV orientations. (c) Extracted resonance frequencies over time for each NV orientation (NV1, NV2, NV3, and NV4) representing magnetic-field projection along each axis. (d) Transformation of resonance frequency differences (Δf_{1-4}) into magnetic-field components (B_x, B_y, B_z) in the sensor's intrinsic reference frame. Comparison of OSCAR-QUBE and MEMS reference magnetometer data. (e) Sequence of reference frame transformation: from the QUBE frame to the ISS frame, to the inertial J2000 frame, to the ECEF frame, and to the final NED frame.

longitudinal, lateral, and vertical directions. In orbit, the ISS frame is in a continuous motion relative to Earth, which provides the reference frame in which the magnetic-field measurements are interpreted. To reconstruct the magnetic-field vector and produce maps, transformations between the sensor, ICF, ISS, and North-East-down (NED) frames are required. Transforming the vector from the ISS frame to the NED frame required a series of intermediate reference frames. The ISS frame is first converted to the Earth-centered inertial (J2000) frame to account for orbital motion, followed by a transformation to the Earth-centered Earth-fixed (CTRS/ECEF) frame, which rotates with the planet. Finally, the vector is projected into the NED frame using the geodetic coordinates of the target

location. This sequence, along with time-stamped attitude data from the ISS, ensures correct interpretation of the space-based magnetic-field measurements and allows for comparison with geomagnetic models. The complete overview of this process is visualized in Fig. 3.

Although the sensor was characterized and the NV-axes calibration was performed, there was an expected pointing error of 4.09° originating as a limitation of the Helmholtz coil system [35] used for calibration. The Helmholtz system consisted of three orthogonal pairs of Helmholtz coils, designed to generate uniform magnetic fields along the X, Y, and Z directions for full vector calibration. This pointing error influences the transformation into the X, Y, and Z components of the magnetic field during the measurements. Additionally, there was no zero-field ground calibration performed. As a result, in-orbit calibration was required. This involved postprocessing of the complete 231 GB in-orbit dataset to extract the magnetic-field variations and statistically infer the optimal transformation parameters, compensating for the absence of on-ground calibration. The measured vector field is aligned to a 3×3 calibration matrix and offset vector. However, this indirect approach introduces additional sources of error.

Despite near continuous coverage provided by the ISS, there were brief periods of data loss caused by EPS rack downtime, communication issues, and similar interruptions. These were in magnetically interesting areas, and as the data was not time stamped on the experiment side, a loss of signal (LOS) and acquisition of signal (AOS) detection system was created to minimize the data loss. In periods where the sensor was measuring but not transferring its data, it labeled it as LOS, to be sent down once the communication was re-established. This LOS data was temporarily stored on an SD card inside the experiment, the maximum data rates were $40 \times 1\,\mathrm{kB/s}$. However, this solution created another complexity in the data-processing pipeline, which was the sorting of data, about 99 million ODMR sweeps. After this step, the peaks were extracted using a peak detection algorithm. After appending GPS data to each packet using time-stamp synchronization, the measurement data was downsampled to 1 Hz by averaging, to match the GPS dataset. The CHAOS-7 and IGRF model data corresponding to GPS and timestamp data were generated and appended to the packet for later comparison. The aforementioned reference frame transformations were conducted, followed by statistical-analysis-based calculations performed in two steps: (1) the field generated by the bias magnet and (2) offsets to match the reference magnetometer, which in turn was calibrated to match the model in the ISS frame. The bias magnet's contribution was approximated by averaging the bias splitting over the mission duration. While this should return the contribution of the magnet exclusively, it can also remove part of the desired external slowly moving variations of the Earth's magnetic field. No full in-orbit calibration of the sensors was performed. Instead, model-based offsets for each axis were applied using a least-squares fit to the IGRF field to enable comparison of trends between measured and model data. This introduces a residual error across the dataset due to natural drift in the Earth's magnetic field over time. Spacecraft-induced magnetic noise (e.g., placement-related noise) was also assessed, though the results are not included in this paper.

F. Data-rejection considerations

During the processing of the dataset, a significant part of measurements were rejected due to several reasons. One reason is the lack of attitude and location data during certain periods of time (approximately 45%). This data was rejected, as the GPS interpolation caused unpredictable behavior. Several measurements during sorting were rejected, due to mismatching of the time stamps. Measurements between 01:00 am and 02:00 am GMT were rejected due to the ICF virus scan, during which the ICF fans are activated on max power, resulting in temperature change of the system and vibrations in the dataset. Furthermore, measurements using either wrong MW settings or laser settings were filtered out (approximately 20%). This resulted in a cleaner dataset for analyzing and producing the magnetic field maps. The rejected data will be further analyzed in a future work. Approximately 32.3% of the total acquired magnetic-field data was deemed usable and subsequently processed.

G. Long-term stability evaluation

The stability of the OSCAR-QUBE sensor was evaluated through longer-term monitoring of parameters influencing the magnetic-field measurements. These indicators of stability include: ODMR parameters (signal contrast, FWHM, SNR, baselines), magnetic-field drift over time, pointing accuracy, and internal temperature fluctuations. The stability of the sensor was assessed by monitoring each of these key indicators over a period of 10 months. To further identify trends and potential degradation, a statistical analysis of the residuals between measured, reference magnetometer, and model magnetic-field data was performed (see Supplemental Material [46]).

III. RESULTS AND DISCUSSION

A. Technical implementation

Here we demonstrate the developed NV-based magnetometer prototype that was implemented as a fully integrated cw ODMR magnetometer system with 1U ($10 \times 10 \times 10\,\mathrm{cm}^3$) form factor. The practical achieved sensitivity of the sensor was $300\,\mathrm{nT}/\sqrt{\mathrm{Hz}}$. This sensitivity was measured using a power spectral density analysis during preflight testing, which can be found in Ref. [35]. The

FIG. 4. OSCAR-QUBE diamond-based magnetometer flown aboard the International Space Station.

OSCAR-QUBE flight model is shown in Fig. 4. The resulting specifications are presented in Table I. These values were determined during ground characterization before launch. The majority of measurements were performed under 27–29 mW laser excitation, microwave power of +26 dBm in a range of 2660–3090 MHz. During the operation phase, measurement parameters were adjusted several times to optimize performance of the magnetometer, which had an influence on the ODMR data, as discussed further in this chapter. The development of the magnetometer went through the full lifecycle of a space project, including design, prototyping, testing, and final integration. The mission was selected in April of 2020 and was delivered for shipping exactly one year later in April of 2021. The experiment was launched on August 29, 2021 and installed inside the ICF on September 2. The sensor was decommissioned in June 2022 and subsequently brought back to Earth for further analysis. During the operation phase, a total of 231 GB of raw data (including ODMR and housekeeping data) was acquired.

TABLE I. OSCAR-QUBE sensor specifications.

Parameters	Value	Comments
Size	1U	$10 \times 10 \times 10\,\mathrm{cm}^3$
Weight	420 g	
Power consumption	5 W	Peak power consumption
dc sensitivity	$<300\,\mathrm{nT}/\sqrt{\mathrm{Hz}}$	Noise spectrum can be found in Refs. [36,47]
Measurement rate	<40 Hz	Vector mode
	<1.3 kHz	Single-axis mode
Dynamic range	1.86 mT	
Nitrogen concentration	14 ppm	⟨100⟩ CVD diamond
NV concentration	2 ppm	⟨100⟩ CVD diamond

B. Performance evaluation

To demonstrate the capability of long-term magnetic-field sensing with the device in harsh conditions, measurements were gathered for a period of 10 months. Figure 5(a) shows the recorded ODMR spectra for the first 8 months of operation aboard the ISS, showing a qualitative assessment of stability of the NV-based magnetometer technology in real space conditions. The photoluminescence signal has been normalized to visually compare the data. As ODMR is the core sensing principle of the technology, its stability directly correlates with the reliability of magnetic-field measurements. Spectrum, theoretical sensitivity of the diamond, baseline signal intensity, contrast, and FWHM of resonance peaks were monitored as indicators of system stability, representing the key ODMR characteristics. Figures 5(b)–5(e) presents the key performance metrics of the magnetometer. Error bars representing standard deviation indicate variability of the dataset over the mission duration. The measurement contrast over the 8-month

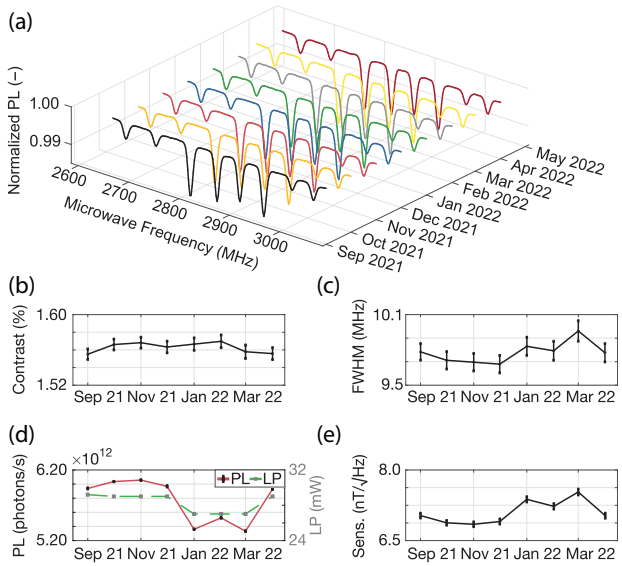

FIG. 5. ODMR measurements and extracted parameters from 8 months of operation aboard the ISS, showing no observable degradation in sensor performance. (a) ODMR spectra displaying eight resonance peaks used for analysis. (b) Evolution of the contrast parameter. (c) Evolution of the linewidth parameter. (d) Evolution of baseline signal and set laser power. (e) Evolution of theoretical calculated sensitivity. Error bars represent the standard deviation across repeated measurements.

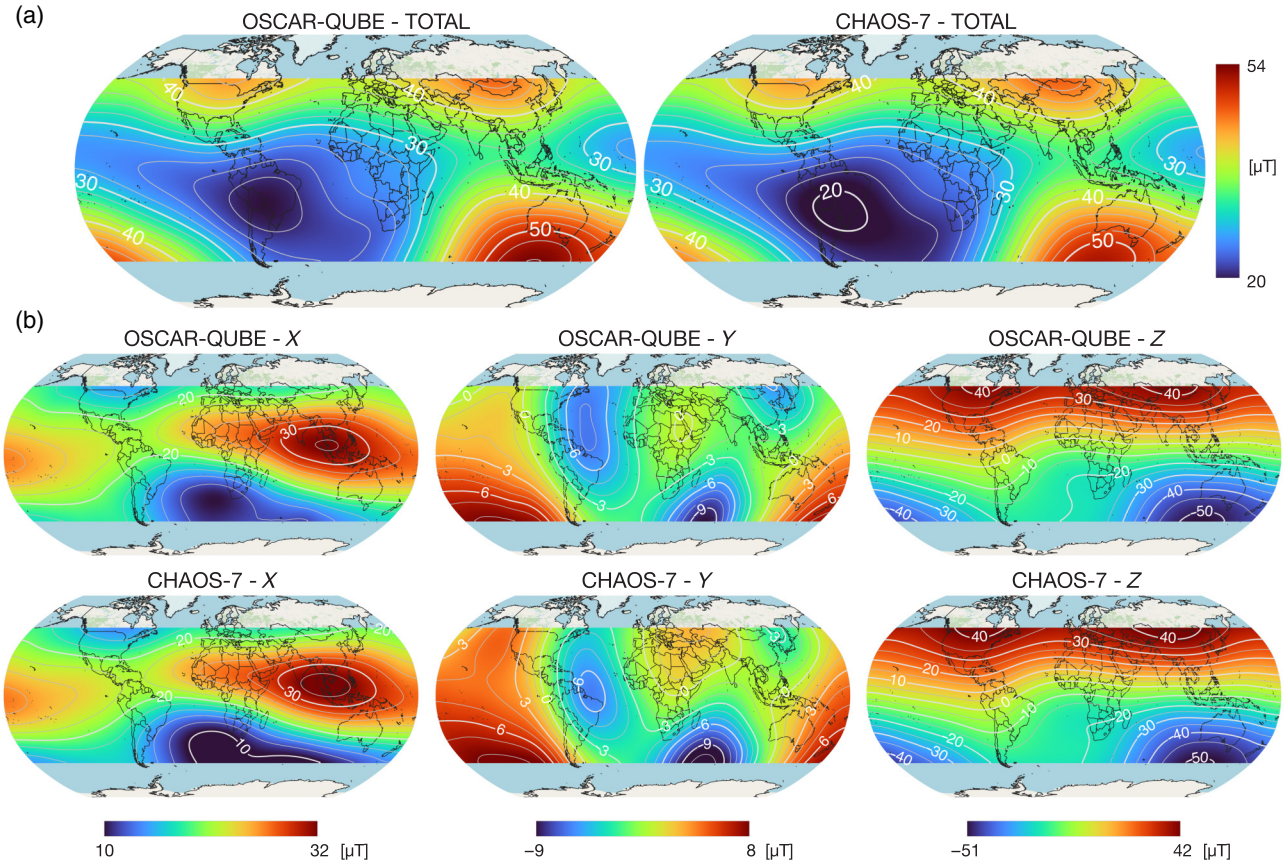

FIG. 6. (Top) Map of the total magnetic-field strength of the earth made from 10 months of data measured using the OSCAR-QUBE sensor (left) onboard the ISS compared to the CHAOS-7 model (right). (Middle and bottom) Comparison of individual magnetic-field components (X, Y, and Z) measured by the OSCAR-QUBE sensor (middle) and their corresponding CHAOS-7 model values (bottom). Overall the maps show strong agreement between measurement and geomagnetic-field model.

period ranged from 1.56% to 1.57%. Across all months, the standard deviation of the contrast was calculated to be ±0.015%, indicating minimal drift of the contrast. The FWHM ranged from 9.68 to 9.96 MHz across the entire mission. The overall standard deviation was ±0.09 MHz. The calculated theoretical sensitivity [Eq. (1)] of the diamond with the OSCAR-QUBE sensor varied between 6.90 nT/$\sqrt{\text{Hz}}$ and 7.60 nT/$\sqrt{\text{Hz}}$, with standard deviation of the monthly averages being ±0.26 nT/$\sqrt{\text{Hz}}$. The second part of the mission shows a change in baseline influencing the performance of the magnetometer, because of a change in laser power. The laser power was changed from 29 to 27 mW, to avoid saturation of the readout subsystem operating at the upper detection limit, resulting in less red fluorescence hence impacting the sensitivity. The ODMR spectra exhibited minimal, if any, shifts in resonance frequency and linewidth, indicating excellent stability. The stable ODMR signal and parameters over the mission duration serves as an initial demonstration of the robustness of the diamond-based magnetometer to long-term operation in a harsh space environment. We further examine the magnetic-field measurements performed aboard the ISS, verifying the agreement with the CHAOS-7 magnetic-field model and demonstrating the successful operation and long-term stability of the diamond-based magnetometer in low Earth orbit. Figure 6 presents the magnetic-field maps derived from the OSCAR-QUBE measurements. The entire dataset acquired over a span of 10 months is displayed. The visualization is realized by averaging the values onto a latitude-longitude grid and then interpolating. Figure 6(a) shows the maps for the total magnetic field and the corresponding map for the CHAOS-7 model. The range of the total measured magnetic-field intensity was between 20 and 54 μT, in agreement with the geomagnetic-field model. Figure 6(b) shows the maps for the individual components (X, Y, and Z in the NED frame) and comparison to CHAOS-7. It showcases that the large-scale features from the measured magnetic-field patterns match the CHAOS-7 model, validating the sensor's vector measurements. Moreover, structures such as the South Atlantic anomaly, a region of locally weakened geomagnetic field over the South Atlantic, can be clearly resolved in the measurement data. The residuals for the maps are presented in the Supplemental Material [46].

TABLE II. Statistical analysis of magnetic-field components.

Component	Mean residuals (nT)	RMSE (nT)	PCC	Within ±2000 nT (%)
Total	701.46	1248.40	0.992	88.91
X	299.35	1205.08	0.993	92.87
Y	−1136.18	1653.91	0.956	74.34
Z	−952.61	1068.23	1.0	97.52

To quantitatively assess the level of agreement between the measured magnetic-field maps and geomagnetic-field model, a statistical analysis was performed for all the field components: total, X, Y, and Z. More specifically the metrics root-mean-square error (RMSE), mean residuals, and Pearson correlation coefficient (PCC) were calculated. The full analysis is shown in Table II.

The measured data demonstrates strong overall agreement with the CHAOS-7 model across most of the components. Particularly total and X component indicate a good agreement with high correlation, low error, and the majority of data within the ±2 μT range (Table II). This threshold was chosen based on the sensor's sensitivity, to allow for both model error and sensor drift. On the other hand, the Y component has good correlation but shows higher RMSE and larger negative mean residual, suggesting systematic offset or discrepancy between both datasets. Regarding the Z component, while showing perfect correlation hence capturing the large-scale structure, there is a discrepancy in the absolute errors, possibly due to local variations causing residual artifacts. Discrepancies

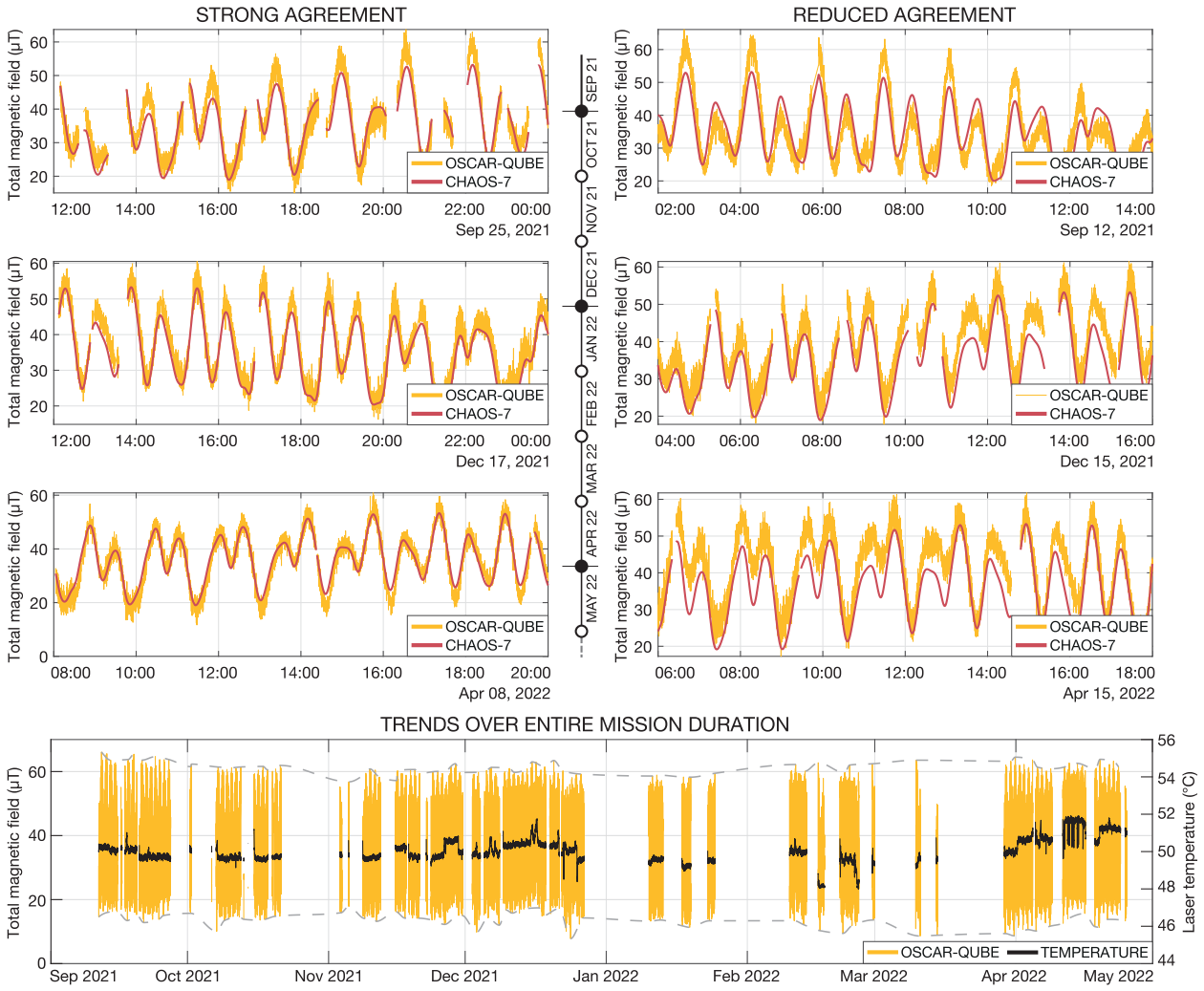

FIG. 7. Total magnetic-field measured by the OSCAR-QUBE sensor throughout the entire mission duration. (Top) Comparison of six selected windows of 12-h periods in beginning, middle, and end of the mission. Selected periods show both close correspondence (left) and noticeable discrepancies (right) between measured data and CHAOS-7 model. (Bottom) Total magnetic-field strength (yellow) compared with laser temperature (black), indicating the influence of temperature on the data. Gaps in plots are due to missing measurement data or missing GPS data. Gray dashed line is the upper and lower envelope of the dataset for eye guidance.

with the model can be due to limitations in sensor sensitivity, calibration accuracy, and spacecraft orientation, all of which can influence the vector components to varying degrees.

Overall, the data measured from space with the diamond-based sensor demonstrates close agreement between the measured maps and geomagnetic-field model data, highlighting the functionality of the technology. While minor deviations are present, these are expected and can be attributed to several potential factors such as calibration errors, temperature instabilities, lower sensor sensitivity in specific axes, spacecraft generated magnetic noise, or possible local effect of the magnetic field. To remove the exact source of these deviations, further optimization of the technology is needed, as well as improved (in-orbit) calibration methodology and noise reduction techniques.

The top part of Fig. 7 showcases a comparison of 12 h between the measured total magnetic field and the CHAOS-7 model. This comparison is shown for month 1 (September 2021), 4 (January 2022), and 8 (April 2022) of the mission. Representative 12-h intervals from these are presented, highlighting both regions of strong correspondence and areas of clear discrepancy between the measured data and the CHAOS-7 model. These highlight that the sensor overall operated accurately, while during certain times overestimating or underestimating the magnetic field of Earth. On top of aforementioned potential effects, temperature can also influence the ODMR data and the system overall (such as the permanent magnet), and can be potentially mitigated by further data processing and the implementation of a temperature correction algorithm in future missions. These will be investigated in a future work. Overall, the measured data is in close agreement with the model. As shown in Table II, approximately 88.91% of the total magnetic-field measurements across the dataset fall within $\pm 2\,\mu$T of the geomagnetic-field model.

The total magnetic-field magnitude over the full mission timeline is shown in Fig. 7(g). The last month of the mission was omitted from the figure as this period was focused on a deeper system evaluation with different operation regimes and parameters being tested, preventing the use of this data for relevant comparison within this study. The data exhibits some minor visible oscillation and drift over the 10 months of measurements. This drift can be compared with the variation of laser temperature shown in black, highlighting a certain influence of temperature instabilities on the measurement system. No significant degradation or anomalies are observed over time, further demonstrating the stability of the instrument in orbit.

To further investigate the behavior of the magnetic-field measurements over time, the total magnetic field was averaged for each day and compared over the entire mission duration. This is shown in Fig. 8. A close agreement

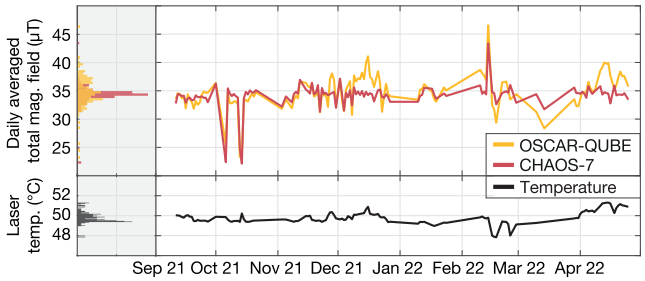

FIG. 8. Daily averaged total magnetic-field strength measured by the OSCAR-QUBE sensor and compared to the geomagnetic-field model CHAOS-7 for the entire mission duration. The data shows good alignment between both datasets, with observable fluctuations over time. The bottom plot shows the laser temperature over the same time, hinting towards possible correlations between sensor temperature and magnetic-field measurements.

between both model and measured data is observed. The CHAOS-7 model has a single mean value of 33.8 μT. The measured dataset shows more variation and also two peaks in the histogram, one around 33.7 μT and the other at 36.4 μT. A first potential source of these variations could be temperature cycling or instabilities. As shown in the bottom panel of Fig. 8, the laser temperature showcases the same spread as seen in the measured magnetic data, highlighting a potential correlation between both. Temperature fluctuations manifest in the ODMR spectrum as a shift of the resonance line, thus influencing the data processing analysis. Although the sensor operated in a thermally controlled environment of the ICF, temperature fluctuations cannot be entirely ruled out. To further investigate the long-term stability of diamond-based quantum sensors, additional temperature monitoring will be conducted. Since NV centers enable both magnetometry and thermometry, this allows for integrated temperature monitoring within the same system. As a result, such quantum magnetometers could be enhanced with self-correction protocols in the future. Besides diamond, temperature also influences the permanent magnet (alignment and magnetization) [48], negatively influencing the measurement data. Other sources, such as magnetic noise, environmental effects, etc., also contribute to the final result and should be mitigated in future missions. In conclusion, the sensor performed exceptionally well in accordance with the ground testing, even though it is a complex system located inside the ISS environment which introduced additional noise. The sensor consistently delivered high-quality data, in agreement with the ground testing, during the entire 10 months of operation. Its operation under these real space conditions highlights the reliability and stability of the system and confirms the viability of diamond-based sensors for future space missions.

IV. CONCLUSION AND OUTLOOK

The work focuses on a diamond-based magnetometer developed as part of the OSCAR-QUBE mission aboard the ISS. It demonstrates the successful reported operation of the diamond-based quantum sensing technology in a space environment for 10 months. The ODMR spectra and their parameters remained stable over the entire mission duration, the deviation for contrast was $\pm 0.015\%$, and FWHM was ± 0.09 MHz. The final sensor had an overall sensitivity of $<300\,\mathrm{nT}/\sqrt{\mathrm{Hz}}$. The acquired magnetic-field maps are in good agreement with the CHAOS-7 model. Minor variations and deviations are present, most likely due to spacecraft-related magnetic noise, calibration errors, lower sensor sensitivity, local magnetic-field effect, or thermal fluctuations. The influence of these events and potential sources of error and mitigation strategies will be further investigated in future work. In-depth investigation of the matching between the acquired data and model shows periods of excellent agreement and periods of less agreement. Temperature influence, degradation of the magnet and magnet alignment are also possible sources of error, an issue that can be mitigated by the implementation of calibration or bias magnetic-field application coils. Future work focuses on testing a passive navigation method using diamond-based sensors onboard ESA Ariane 6 rocket (OSCAR-QUBE+), and on further integration and sensitivity optimization of the technology. In conclusion, this work demonstrates the potential of this novel technology as a reliable tool for magnetic-field measurements in the space environment, highlighting its suitability for future space missions.

ACKNOWLEDGMENTS

The OSCAR-QUBE project was developed within the framework of the European Space Agency (ESA) Academy "Orbit Your Thesis!" program, which provided the opportunity to design, qualify, and test the experiment in a microgravity environment. The authors acknowledge the support of Space Applications Services during the design, qualification, and operation phases, as well as hosting the experiment aboard the International Space Station within the ICECubes Facility for extended mission duration. The authors are grateful to Melexis, POM Limburg, Select System s.r.o., and Element Six for their support in facilitating the retrieval of the device from the ISS, and providing materials or services in course of the project. Special thanks are due to Nigel Savage (ESA) for his valuable guidance throughout the Orbit Your Thesis! program. The authors also acknowledge the scientific insights and support provided by their ELGRA mentors, Marco Braibanti (ESA) and Sven Hermann (ZARM). The team thanks Koen De Beule (ESA) and Piotr Skrzypek (ESA) for their advice and support during various stages of the project. Further appreciation goes to Michal Gulka (IOCB Prague) for constructive feedback, technical guidance, and support throughout the manuscript writing process. The authors also thank Anna Ermakova (UHasselt/BIRA) for her contributions to manuscript preparation, data processing, and scientific interpretation. The authors acknowledge the use of infrastructure and testing facilities provided by UHasselt and IUMAT, which were essential for sensor verification and mission integration, as well as Makerspace PXL/UHasselt for technical support. J.H. acknowledges support from the Research Foundation – Flanders (FWO), Grant No. 11D6620N, and the Agency for Innovation and Entrepreneurship (VLAIO), Grant No. HBC.2022.0211. Y.B. acknowledges the Special Research Fund (BOF) of Hasselt University, Grant No. BOF23OWB36.

DATA AVAILABILITY

The data that support the findings of this article are not publicly available upon publication because it is not technically feasible and/or the cost of preparing, depositing, and hosting the data would be prohibitive within the terms of this research project. The data are available from the authors upon reasonable request.

[1] Nils Olsen and Claudia Stolle, Satellite geomagnetism, Annu. Rev. Earth Planet. Sci. **40**, 441 (2012).

[2] Nils Olsen, G. Hulot, and T. J. Sabaka, Measuring the Earth's magnetic field from space: Concepts of past, present and future missions, Space Sci. Rev. **155**, 65 (2010).

[3] Mario H. Acuna, Space-based magnetometers, Rev. Sci. Instrum. **73**, 3717 (2002).

[4] Gauthier Hulot, C. C. Finlay, C. G. Constable, Nils Olsen, and Mioara Mandea, The magnetic field of planet earth, Space Sci. Rev. **152**, 159 (2010).

[5] Eigil Friis-Christensen, Hermann Lühr, and Gauthier Hulot, Swarm: A constellation to study the Earth's magnetic field, Earth Planets Space **58**, 351 (2006).

[6] Jean-Michel Leger, François Bertrand, Thomas Jager, Matthieu Le Prado, Isabelle Fratter, and Jean-Claude Lalaurie, Swarm absolute scalar and vector magnetometer based on helium 4 optical pumping, Procedia Chem. **1**, 634 (2009).

[7] Jean-Michel Léger, Thomas Jager, François Bertrand, Gauthier Hulot, Laura Brocco, Pierre Vigneron, Xavier Lalanne, Arnaud Chulliat, and Isabelle Fratter, In-flight performance of the absolute scalar magnetometer vector mode on board the swarm satellites, Earth Planets Space **67**, 57 (2015).

[8] Bin Zhou, Bingjun Cheng, Xiaochen Gou, Lei Li, Yiteng Zhang, Jindong Wang, Werner Magnes, Roland Lammegger, Andreas Pollinger, Michaela Ellmeier, *et al.*, First in-orbit results of the vector magnetic field measurement of the high precision magnetometer onboard the China SEISMO-electromagnetic satellite, Earth Planets Space **71**, 119 (2019).

[9] Yi Jiang, Christopher C. Finlay, Nils Olsen, Lars Tøffner-Clausen, Qing Yan, and Keke Zhang, Macau scientific satellite-1 initial magnetic field model, Geophys. Res. Lett. **51**, e2024GL112305 (2024).

[10] Gauthier Hulot, Jean-Michel Léger, Pierre Vigneron, Thomas Jager, François Bertrand, Pierdavide Coïsson, Pierre Deram, Axel Boness, Linda Tomasini, and Benoit Faure, in *IGARSS 2018-2018 IEEE International Geoscience and Remote Sensing Symposium* (IEEE, Valencia, Spain, 2018), pp. 6320–6323.

[11] Gauthier Hulot, Jean-Michel Leger, Lasse B. N. Clausen, Florian Deconinck, Pierdavide Coïsson, Pierre Vigneron, Patrick Alken, Arnaud Chulliat, Christopher C. Finlay, Alexander Grayver, *et al*., in *EGU21-The EGU General Assembly 2021* (Vienne, Austria & European Geosciences Union, 2021).

[12] NASA, MagQuest – NASA, (2025), accessed: July 01, 2025, https://www.nasa.gov/general/magquest/.

[13] Christopher C. Finlay, Clemens Kloss, Nils Olsen, Magnus D. Hammer, Lars Tøffner-Clausen, Alexander Grayver, and Alexey Kuvshinov, The CHAOS-7 geomagnetic field model and observed changes in the South Atlantic anomaly, Earth Planets Space **72**, 156 (2020).

[14] Christopher C. Finlay, Stefan Maus, Ciarán D. Beggan, Mohamed Hamoudi, Frank J. Lowes, Nils Olsen, and Erwan Thébault, Evaluation of candidate geomagnetic field models for IGRF-11, Earth Planets Space **62**, 787 (2010).

[15] James S. Bennett, Brian E. Vyhnalek, Hamish Greenall, Elizabeth M. Bridge, Fernando Gotardo, Stefan Forstner, Glen I. Harris, Félix A. Miranda, and Warwick P. Bowen, Precision magnetometers for aerospace applications: A review, Sensors **21**, 5568 (2021).

[16] Pavel Ripka, *Magnetic Sensors and Magnetometers* (Artech House, 2021), ISBN: 978-1-630-81742-8.

[17] Kai-Mei C. Fu, Geoffrey Z. Iwata, Arne Wickenbrock, and Dmitry Budker, Sensitive magnetometry in challenging environments, AVS Quantum Sci. **2**, 044702 (2020).

[18] Nils Olsen, Giuseppe Albini, Jerome Bouffard, Tommaso Parrinello, and Lars Tøffner-Clausen, Magnetic observations from cryosat-2: Calibration and processing of satellite platform magnetometer data, Earth Planets Space **72**, 48 (2020).

[19] YiXin Qiu, Ying Zhang, YaSong Ge, AiMin Du, ShuQuan Sun, Lin Zhao, Hao Luo, Lei Wang, Lin Tian, Zhi Li, *et al*., In-flight calibration of the fluxgate magnetometer on Macau Science satellite-1, Earth Planet. Phys. **9**, 511 (2025).

[20] Lars Tøffner-Clausen, Vincent Lesur, Nils Olsen, and Christopher C. Finlay, In-flight scalar calibration and characterisation of the swarm magnetometry package, Earth Planets Space **68**, 129 (2016).

[21] L. N. S. Alconcel, P. Fox, P. Brown, T. M. Oddy, E. L. Lucek, and C. M. Carr, An initial investigation of the long-term trends in the fluxgate magnetometer (FGM) calibration parameters on the four cluster spacecraft, Geosci. Instrum. Methods Data Syst. **3**, 95 (2014).

[22] Alex Paul Hoffmann, Mark B. Moldwin, Brady P. Strabel, and Lauro V. Ojeda, Enabling boomless cubesat magnetic field measurements with the quad-mag magnetometer and an improved underdetermined blind source separation algorithm, J. Geophys. Res.: Space Phys. **128**, e2023JA031662 (2023).

[23] Thomas Wolf, Philipp Neumann, Kazuo Nakamura, Hitoshi Sumiya, Takeshi Ohshima, Junichi Isoya, and Jörg Wrachtrup, Subpicotesla diamond magnetometry, Phys. Rev. X **5**, 041001 (2015).

[24] Ricardo S. Sussmann, *CVD Diamond for Electronic Devices and Sensors* (John Wiley & Sons, 2009), ISBN: 978-0-470-74039-2.

[25] John F. Barry, Jennifer M. Schloss, Erik Bauch, Matthew J. Turner, Connor A. Hart, Linh M. Pham, and Ronald L. Walsworth, Sensitivity optimization for NV-diamond magnetometry, Rev. Mod. Phys. **92**, 015004 (2020).

[26] Jixing Zhang, Lixia Xu, Guodong Bian, Pengcheng Fan, Mingxin Li, Wuming Liu, and Heng Yuan, Diamond nitrogen-vacancy center magnetometry: Advances and challenges, arXiv:2010.10231.

[27] Jennifer M. Schloss, John F. Barry, Matthew J. Turner, and Ronald L. Walsworth, Simultaneous broadband vector magnetometry using solid-state spins, Phys. Rev. Appl. **10**, 034044 (2018).

[28] Philipp Neumann, Ingmar Jakobi, Florian Dolde, Christian Burk, Rolf Reuter, Gerald Waldherr, Jan Honert, Thomas Wolf, Andreas Brunner, Jeong Hyun Shim, *et al*., High-precision nanoscale temperature sensing using single defects in diamond, Nano Lett. **13**, 2738 (2013).

[29] Felix M. Stürner, Andreas Brenneis, Thomas Buck, Julian Kassel, Robert Rölver, Tino Fuchs, Anton Savitsky, Dieter Suter, Jens Grimmel, Stefan Hengesbach, *et al*., Integrated and portable magnetometer based on nitrogen-vacancy ensembles in diamond, Adv. Quantum Technol. **4**, 2000111 (2021).

[30] Akihiro Kuwahata, Takahiro Kitaizumi, Kota Saichi, Takumi Sato, Ryuji Igarashi, Takeshi Ohshima, Yuta Masuyama, Takayuki Iwasaki, Mutsuko Hatano, Fedor Jelezko, *et al*., Magnetometer with nitrogen-vacancy center in a bulk diamond for detecting magnetic nanoparticles in biomedical applications, Sci. Rep. **10**, 2483 (2020).

[31] Yuta Kainuma, Yuji Hatano, Takayuki Shibata, Naota Sekiguchi, Akimichi Nakazono, Hiromitsu Kato, Shinobu Onoda, Takeshi Ohshima, Mutsuko Hatano, and Takayuki Iwasaki, Compact and stable diamond quantum sensors for wide applications, Adv. Quantum Technol. **7**, 2300456 (2024).

[32] Mohamed I. Ibrahim, Christopher Foy, Dirk R. Englund, and Ruonan Han, High-scalability CMOS quantum magnetometer with spin-state excitation and detection of diamond color centers, IEEE J. Solid-State Circuits **56**, 1001 (2021).

[33] Jens Pogorzelski, Ludwig Horsthemke, Jonas Homrighausen, Dennis Stiegekötter, Markus Gregor, and Peter Glösekötter, Compact and fully integrated led quantum sensor based on NV centers in diamond, Sensors **24**, 743 (2024).

[34] Xiao Peng, Fei Xie, Yaochen Zhu, Xin Luo, Qihui Liu, Dan Wang, Yuqiang Hu, Jiachen Han, Lingyun Li, Jianping Liu, *et al*., A highly integrated three-axis vector diamond quantum magnetometer with a compact electrical package, Appl. Phys. Lett. **126**, 081101 (2025).

[35] Jaroslav Hruby, Siemen Achten, Musa Aydogan, Sam Bammens, Yarne Beerden, Boo Carmans, Dries Hendrikx, Jeffrey Gorissen, Teoman Köseoglu, Jens Mannaerts, Remy Vandebosch, Siemen Vandervoort, Sebastiaan Vanspauwen, and Milos Nesladek, in *72nd International Astronautical Congress* (Dubai, UAE, 2021).

[36] Boo Carmans, Siemen Achten, Musa Aydogan, Sam Bammens, Yarne Beerden, Dries Hendrikx, Jeffrey Gorissen, Teoman Köseoglu, Jens Mannaerts, Remy Vandebosch, Siemen Vandervoort, Sebastiaan Vanspauwen, Milos Nesladek, and Jaroslav Hruby, in *4th Symposium on Space Educational Activities* (Universitat Politècnica de Catalunya, Barcelona, Spain, 2022).

[37] Marcus W. Doherty, Neil B. Manson, Paul Delaney, Fedor Jelezko, Jörg Wrachtrup, and Lloyd C. L. Hollenberg, The nitrogen-vacancy colour centre in diamond, Phys. Rep. **528**, 1 (2013).

[38] Loïc Rondin, Jean-Philippe Tetienne, Thomas Hingant, Jean-François Roch, Patrick Maletinsky, and Vincent Jacques, Magnetometry with nitrogen-vacancy defects in diamond, Rep. Prog. Phys. **77**, 056503 (2014).

[39] Edlyn V. Levine, Matthew J. Turner, Pauli Kehayias, Connor A. Hart, Nicholas Langellier, Raisa Trubko, David R. Glenn, Roger R. Fu, and Ronald L. Walsworth, Principles and techniques of the quantum diamond microscope, Nanophotonics **8**, 1945 (2019).

[40] Emilie Bourgeois, A. Jarmola, P. Siyushev, Michal Gulka, Jaroslav Hruby, Fedor Jelezko, D. Budker, and Milos Nesladek, Photoelectric detection of electron spin resonance of nitrogen-vacancy centres in diamond, Nat. Commun. **6**, 8577 (2015).

[41] Michal Gulka, Emilie Bourgeois, Jaroslav Hruby, Petr Siyushev, Georg Wachter, Friedrich Aumayr, Philip R. Hemmer, Adam Gali, Fedor Jelezko, Michael Trupke, *et al*., Pulsed photoelectric coherent manipulation and detection of n-v center spins in diamond, Phys. Rev. Appl. **7**, 044032 (2017).

[42] Jaroslav Hruby, Emilie Bourgeois, Milos Nesladek, and Ward De Ceuninck, Magnetometer sensor with negatively charged nitrogen-vacancy centers in diamond, U.S. Patent 10,274,551 (2019).

[43] Jaroslav Hruby, Michal Gulka, Massimo Mongillo, Iuliana P. Radu, Michael V. Petrov, Emilie Bourgeois, and Milos Nesladek, Magnetic field sensitivity of the photoelectrically read nitrogen-vacancy centers in diamond, Appl. Phys. Lett. **120**, 162402 (2022).

[44] Jan Jeske, Jared H. Cole, and Andrew D. Greentree, Laser threshold magnetometry, New J. Phys. **18**, 013015 (2016).

[45] S. M. Graham, A. T. M. A. Rahman, L. Munn, R. L. Patel, A. J. Newman, C. J. Stephen, G. Colston, A. Nikitin, A. M. Edmonds, D. J. Twitchen, M. L. Markham, and G. W. Morley, Fiber-coupled diamond magnetometry with an unshielded 30 Pt/Hz sensitivity, Phys. Rev. Appl. **19**, 044042 (2023).

[46] See Supplemental Material at http://link.aps.org/supplemental/10.1103/483m-8hfc for additional statistics and comparisons to geomagnetic-field models.

[47] Yarne Beerden, Remy Vandebosch, Anna Ermakova, Milos Nesladek, and Jaroslav Hruby, Long-term stability assessment of quantum diamond magnetometers in low Earth orbit, *IGARSS 2024-2024 IEEE International Geoscience and —Remote Sensing Symposium* (IEEE, Athens, Greece, 2024), pp. 465–468.

[48] Hu-Lin Wu, Zhi-Mei Long, Kai-Qiang Song, Chao-Qun Li, Da-Long Cong, Bin Shao, Xiao-Wei Liu, and Yi-Long Ma, The effect of temperature cycling on the magnetic degradation and microstructure of a Zn-coated NdFeB magnet, Coatings **12**, 660 (2022).